
Learning Global and Local Features in Pretrained Remote Sensing Models

Gabriel Tseng^{*123} Anthony Fuller^{*4} Marlena Reil¹² Henry Herzog³ Patrick Beukema³ Favyen Bastani³
 James R. Green⁴ Evan Shelhamer⁵ Hannah Kerner^{†6} David Rolnick^{†12}

Abstract

From crop mapping to flood detection, machine learning in remote sensing has a wide range of societally beneficial applications. The commonalities between remote sensing data in these applications present an opportunity for pretrained machine learning models tailored to remote sensing to reduce the labeled data and effort required to solve individual tasks. However, such models must be: (i) flexible enough to ingest input data of varying sensor modalities and shapes (i.e., of varying spatial and temporal dimensions), and (ii) able to model Earth surface phenomena of varying scales and types. To solve this gap, we present Galileo, a family of pretrained remote sensing models designed to flexibly process multimodal remote sensing data. We also introduce a novel and highly effective self-supervised learning approach to learn both large- and small-scale features, a challenge not addressed by previous models. Our Galileo models obtain state-of-the-art results across diverse remote sensing tasks.

1. Introduction

Machine learning is increasingly being used to analyze remote sensing (RS) data across a wide variety of societally important problems, such as agricultural analyses for food security (Kerner et al., 2020) and flood detection for rapid disaster response (Frame et al., 2024). Labels for these applications can be expensive or difficult to acquire (Kebede et al., 2024), motivating recent research into pretrained RS models that can produce accurate insights even with few labels. The commonalities across RS data and tasks here present an advantage, but individual tasks nonetheless present a diversity of specific requirements. Specifically, practitioners need ML models for remote sensing to ❶ flexibly process many

different modalities and input shapes (where we define input shape as $[\text{height} \times \text{width} \times \text{timesteps} \times \text{modalities}]$), and ❷ model phenomena which occur at very different scales.

Different RS applications may require very different inputs, but which inputs are best may not be obvious *a priori*. In addition, data may not always be available, for reasons ranging from the temporary unavailability of a satellite (ESA, 2023) to cloud cover (Coluzzi et al., 2018) to revisit periods for different satellites. This requires our models to ❶ **flexibly process different modalities and input shapes**. For example, to support timely predictions when detecting fishing vessels, Beukema et al. (2023) leverage a range of modalities ranging from optical to synthetic aperture radar (SAR) to nightlights. Achieving strong performance with these modalities requires different input shapes; for example, models benefited from seeing historical imagery when processing SAR data but not optical data. Similarly, Kruse et al. (2023) found that processing RS data *first* as single-timestep imagery, and *then* as pixel-timeseries was optimal when detecting plastic waste.

In addition, ❷ **RS phenomena occur at very different scales**. For example, practitioners use machine learning and RS to map kilometer-scale glaciers which persist for decades (Baraka et al., 2020) and detect meter-scale maritime vessels which are extremely transient in time (Beukema et al., 2023). Single applications can span a huge range of scales; for example, plastic waste sites can range in size from 1,000 m² to 40,000 m² (Kruse et al., 2023), requiring models to identify phenomena across these scales to accurately detect these sites. Similarly, marine phenomena can range from a few isolated pixels (for marine debris) to large contiguous areas (for sediment-laden water) (Kikaki et al., 2024).

We address these challenges by proposing a new family of pretrained RS models called “Galileo” (Global and Local Flexible Earth Observation models). We develop a highly multimodal dataset that varies in space and time to train these models, and we modify the ViT architecture (Dosovitskiy et al., 2021) to process this dataset. We present a novel self-supervised learning (SSL) algorithm to learn useful representations of small- and large-scale features. Our algorithm combines two training objectives: one makes predictions in (essentially) the pixel space, and the other makes

^{*}Equal contribution [†]Equal Supervision ¹Mila – Quebec AI Institute ²McGill University ³Allen Institute for AI (Ai2) ⁴Carleton University ⁵University of British Columbia ⁶Arizona State University. Correspondence to: Gabriel Tseng <gabriel.tseng@mail.mcgill.ca>.

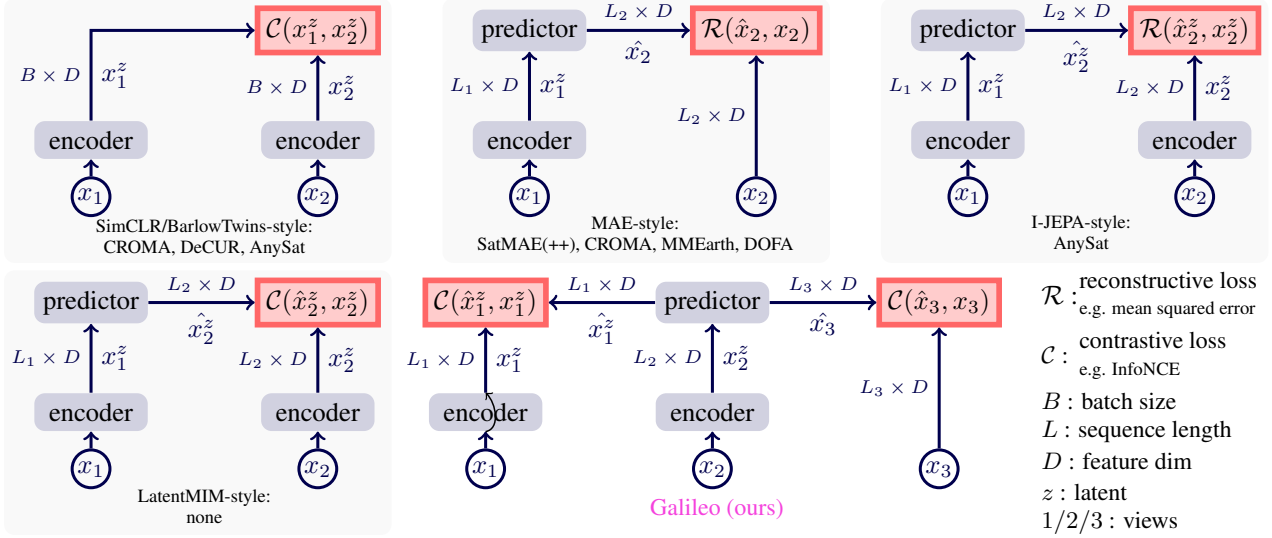


Figure 1. *SSL for RS*. **Top left:** Attracts representations originating from the same sample and repels representations from other samples. **Top center:** Predicts pixels of hidden patches. **Top right:** Predicts representations of hidden patches. **Bottom left:** Attracts representations originating from the same patch and repels representations from other patches. **Galileo (ours):** Our method simultaneously attracts varied-level representations originating from the same patch and repels elsewhere — and attracts pixel predictions originating from the same patch and repels elsewhere. This strategy encourages learning global *and* local features.

predictions in the latent space (Figure 1). We show that these dual objectives are complementary and necessary to improve training stability and achieve good performance across all task scales.

We demonstrate the efficacy of our Galileo models via an extensive benchmarking suite, covering many applications, domains, and RS data types. Fair comparison of RS models is challenging (Corley et al., 2024). To achieve this, we run hundreds of experiments across 16 pretrained RS baselines to robustly compare with existing methods.

2. Multi-modal & Multi-scale Self-Supervision

We aim to pretrain a model that can be applied to a range of RS tasks, even when few labels are available. This requires that we can (i) process many different modalities, (ii) ingest varying input shapes, and (iii) model phenomena that occur at very different scales.

To train a model with capabilities for multimodal processing and input shape flexibility, we first build a pretraining dataset where each training instance includes data for multiple RS modalities, and captures data across a suitably large spatial and temporal range. During model pretraining, we subsample modalities and input shapes (subsetting space and time) from this dataset, such that the resulting model can process multi-scale and multimodal RS data.

However, a traditional ViT architecture expects samples to share the same modalities and input shapes. We therefore

adapt the ViT architecture to ingest arbitrary subsets of modalities, with varying input shapes.

Most existing SSL algorithms have been developed to be effective on natural imagery rather than RS data. We therefore develop a novel SSL algorithm that learns strong representations of both: (i) large objects and lower-frequency features, and (ii) tiny objects and high-frequency features. We achieve this by integrating two complementary algorithms, each specialized for a different scale of feature extraction.

2.1. Achieving Flexibility via the Data and Architecture

2.1.1. COLLECTING DIVERSE PRETRAINING DATA

We collect a large, globally sampled pretraining dataset of 127,155 training instances. Section B.1 describes our dataset sampling process. We include a wide range of RS inputs to serve diverse applications. A training instance consists of 4 types of data covering 9 RS data modalities. We select these modalities based on their uses in past machine learning for remote sensing efforts (Van Tricht et al., 2023; Beukema et al., 2023; Poggio et al., 2021).

We group the modalities by whether they vary in space, time, both, or neither. A single instance consists of 24 monthly timesteps and 96×96 pixels at a 10m/pixel resolution.

Space-time varying data. These data consist of imagery acquired by Sentinel-1 & -2 satellites. For Sentinel-1, we take the VV and VH polarizations; and for Sentinel-2, we take all bands except the B1, B9 and B10 bands. All bands

Table 1. A comparison of model performance and model flexibility. **Performance** is measured via rankings (where lower numbers are better) on image tasks in Tables 13, 14 & 15 and pixel-timeseries tasks in Table 6. For clarity, we select the best architecture per method; full rankings are available in Table 16. **Flexibility** is measured by documenting which inputs are supported by the models: MultiSpectral (MS), Synthetic Aperture Radar (SAR), additional Remote Sensing modalities (+modalities), inputs with spatial dimensions and inputs with more than 1 or 4 timesteps. The Galileo models are both the best performing and the most flexible models. In particular, Galileo-Base is the best performing model when compared to both image-specialized models and pixel-timeseries specialized models.

Method	Arch.	Rank ↓		Supported Inputs					
		Images	Pixel-timeseries	MS	SAR	+modalities	Spatial dims	> 1 timestep	> 4 timesteps
SatMAE	ViT-Large	10.4	N/A	✓			✓		
SatMAE++	ViT-Large	10.9	N/A	✓			✓		
CROMA	ViT-Base	<u>4.3</u>	N/A	✓	✓		✓		
SoftCon	ViT-Base	5.9	N/A	✓	✓		✓		
DOFA	ViT-Large	9.4	N/A	✓	✓		✓		
Satlas	Swin-Tiny	12.9	N/A	✓			✓	✓	
MMEarth	CNN-atto	12.3	N/A	✓			✓		
DeCUR	ViT-Small	8.3	N/A	✓	✓		✓		
Prithvi 2.0	ViT-Large	11.7	N/A	✓			✓	✓	
AnySat	ViT-Base	11.1	4.5	✓	✓	✓	✓	✓	✓
Presto	ViT-Presto	N/A	3.0	✓	✓	✓		✓	✓
Galileo	ViT-Nano	10.9	3.5	✓	✓	✓	✓	✓	✓
Galileo	ViT-Tiny	6.4	<u>2.3</u>	✓	✓	✓	✓	✓	✓
Galileo	ViT-Base	3.0	1.8	✓	✓	✓	✓	✓	✓

are resampled to a 10m/pixel resolution. We also include NDVI (Tucker, 1979) from Sentinel-2 as an input.

Space varying data. These data consist of elevation and slope captured by the Shuttle Radar Topography Mission (NASA JPL, 2000), which are constant in time; Dynamic World land cover map probabilities (Brown et al., 2022), averaged over time for temporal consistency; and World Cereal agricultural land cover maps (Van Tricht et al., 2023).

Time varying data. These data consist of precipitation and temperature from the ERA5 dataset (Hersbach et al., 2020); climate water deficit, soil moisture, and actual evapotranspiration from TerraClimate (Abatzoglou et al., 2018); and VIIRS nighttime lights (Elvidge et al., 2017). Although these modalities vary in space as well, their spatial resolution (ERA5 has a spatial resolution of tens of kilometres per pixel) means we treat them as static in space from the perspective of a single instance.

Static data. These data consist of population estimates from the LandScan dataset (Dobson et al., 2000), the spatial location of the instance, defined by its central latitude and longitude, Dynamic World classes spatially averaged over the instance, and World Cereal agricultural land cover maps spatially averaged over the instance. We include the averaged Dynamic World and World Cereal inputs in addition to the space-varying inputs.

2.1.2. ARCHITECTING A ViT FOR ALL INPUTS

We require a model for the wide range of modalities and input shapes in our dataset to handle the variety of RS data inputs (Section 2.1.1). Transformers are general architectures, but still require tokenization strategies to handle the varied input dimensions of space, time, and modality.

We adapt the ViT (Dosovitskiy et al., 2021) architecture to ingest channel groups and *variable* input shapes and timesteps, as follows:

Patchification and Channel-group projections. We group all inputs described in Section 2.1.1 into “channel-groups” when projecting the input to the encoder dimension, where a channel-group combines semantically cohesive channels (e.g. the RGB bands from Sentinel-2). We patchify — i.e., split the input tensor into spatial squares, timesteps, and channel groups — and project our inputs to the encoder dimension D using the following transformations: (i) Space-time data, $\mathbb{R}^{H \times W \times T \times C} \rightarrow \mathbb{R}^{\frac{H}{P} \cdot \frac{W}{P} \cdot T \cdot G \times D}$, H is the height, W is the width, P is the patch size (in pixels per side), T is the timesteps, C are the channels, G are the channel groups. (ii) Space data, $\mathbb{R}^{H \times W \times C} \rightarrow \mathbb{R}^{\frac{H}{P} \cdot \frac{W}{P} \cdot G \times D}$, (iii) Time data, $\mathbb{R}^{T \times C} \rightarrow \mathbb{R}^{T \cdot G \times D}$, and (iv) Static data, $\mathbb{R}^C \rightarrow \mathbb{R}^{G \times D}$.

Token Embeddings. After these linear projections, our encoder creates spatial and temporal sinusoidal position embeddings, learnable channel embeddings, and month embeddings to enable seasonal reasoning; we denote these token position embeddings as $\mathbf{e} \in \mathbb{R}^{L \times D}$, where L is the token sequence length. Our encoder adds these embeddings

to the linear projections, previously computed. It concatenates all channel groups along the sequence dimension — forming our input sequence, $\mathbf{x} \in \mathbb{R}^{L \times D}$. Importantly, our approach is robust to the presence and varying lengths of channel group sequences.

Flexible input shapes.

We adopt resizable patch embeddings (Beyer et al., 2023). This method resizes the weights of the ViT’s linear projection layer, so that varying patch sizes P can be projected into the encoder dimension. Since each token can now represent different spatial scales, we dynamically adjust the spatial positional embedding frequencies to match the spatial scale, following Reed et al. (2023)’s “Ground Sample Distance Positional Encodings.”: 2D position embeddings are interpolated by a factor of $\frac{P}{H} = \frac{P}{W}$.

2.2. Learning global and local features via SSL

Objects in RS data can range in size from a single pixel to hundreds or thousands of pixels. A single pretraining task is unlikely to capture this huge range in feature size, which we evidence through illustrative experiments. We introduce a novel algorithm that combines two objectives: one to learn local features and the other to learn global features.

Our general latent prediction framework is inspired by Assran et al. (2023), Garrido et al. (2024), and Wei et al. (2024), and operates as follows: (i) Given a batch of samples, we construct two *different* views of each sample, $\mathbf{x}_1 \in \mathbb{R}^{L_1 \times D}$ and $\mathbf{x}_2 \in \mathbb{R}^{L_2 \times D}$. (ii) Our “online” encoder computes patch encodings $\mathbf{z}_1 = \mathbf{E}(\mathbf{x}_1)$, while our “target” encoder — an exponential moving average of the online encoder — computes target patch encodings $\mathbf{z}_2 = \mathbf{E}_{\text{EMA}}(\mathbf{x}_2)$. (iii) A predictor transformer \mathbf{P} receives the target view’s position, time, month, and channel group embeddings $\mathbf{e}_2 \in \mathbb{R}^{L_2 \times D}$ as placeholder queries and predicts patch encodings $\mathbf{p} \in \mathbb{R}^{L_2 \times D}$ by cross-attending to the online patch encodings, i.e., $\mathbf{p} = \mathbf{P}(\mathbf{e}_2, \mathbf{z}_1)$. (iv) The predictions \mathbf{p} and targets \mathbf{z}_2 are compared to compute a loss $\mathcal{L}(\mathbf{p}, \mathbf{z}_2)$ that updates the online encoder.

2.2.1. LEARNING GLOBAL FEATURES

Our global algorithm learns coarse-grained, lower-frequency features suited for classification applications. We modify our general latent prediction framework as follows:

Target Depth. Target patch encodings are typically extracted from the target view through the *entire* target encoder. Some RS modalities (e.g., Dynamic World landcover classes) map closely to downstream tasks (e.g., landcover classification). These inputs may not need to be heavily processed (deeply encoded) to be useful targets. To account for the variable processing level of RS inputs, we compute targets by saving token representations after the ℓ^{th} layer,

where ℓ varies by modality. We select ℓ based on each modality’s abstraction level: pseudo-labels use only linear projections (no encoder layers), Sentinel-1 and Sentinel-2 use all encoder layers, and other channels use half the encoder layers. We denote our level-specific target encoder as $\mathbf{E}_{\text{EMA}}^\ell$.

Loss function. I-JEPA (Assran et al., 2023) and Image World Model (Garrido et al., 2024) compute the mean-squared error (MSE) between predictions and targets. LatentMIM demonstrated superior performance via the “Patch Discrimination” (PatchDisc) loss (Wei et al., 2024), which discriminates between tokens in a sample. To encourage globally discriminative representations, we extend the PatchDisc loss to better discriminate samples in a batch. We define our new loss, called AllDisc, below (note this is equivalent to PatchDisc if the $\sum_{i'}^B$ summation is removed):

$$\mathcal{L}(\mathbf{u}, \mathbf{v}) = \frac{-\tau}{B} \sum_i^B \frac{1}{L_i} \sum_j^{L_i} \log \frac{\exp(\text{sim}(\mathbf{u}_{i,j}, \mathbf{v}_{i,j})/\tau)}{\sum_{i'}^B \sum_{j'}^{L_{i'}} \exp(\text{sim}(\mathbf{u}_{i,j}, \mathbf{v}_{i',j'})/\tau)}$$

with the softmax temperature τ , the sample index i , the batch size B , the token index j , the number of tokens in the i^{th} sample L_i , and the l_2 normalized dot product $\text{sim}(\mathbf{u}, \mathbf{v}) = \mathbf{u}^\top \mathbf{v} / \|\mathbf{u}\| \|\mathbf{v}\|$. Our global loss is:

$$\mathcal{L}_{\text{global}} = \text{AllDisc}(\mathbf{P}(\mathbf{e}_2, \mathbf{E}(\mathbf{x}_1)), \text{sg}(\mathbf{E}_{\text{EMA}}^\ell(\mathbf{x}_2)))$$

where sg is the stop-gradient operation.

Masking Strategy. Structured or contiguous masking increases the distance between online and target tokens. This reduces the ability for the online encoder and predictor to locally interpolate between online (“visible”) tokens to predict the target token’s representation. “Space masking” samples masks across space while maintaining consistency across channel groups and time; “time masking” does the same across time while maintaining consistency across channel groups and space. We alternate between the two during pre-training (see complete masking details in Appendix A.1.1).

2.2.2. LEARNING LOCAL FEATURES

Our local algorithm learns fine-grained, higher-frequency features suited for segmentation applications. We modify our general latent prediction framework as follows:

Target Depth. All prior latent prediction methods target patch representations, rather than pixels, to encourage the encoder to ignore “low-level” image details. While pixel-level details are usually irrelevant in natural imagery, individual pixels can contain essential details in RS. Therefore, we target the lowest representation level: the pixel space. To achieve this with a contrastive objective, we compute targets using the target encoder’s linear projection, $\mathbf{E}_{\text{EMA}}^{\text{proj}}$, *skipping all transformer blocks*.

Loss Function. MAE (He et al., 2022) computes the MSE between predicted and hidden pixels. Although this encour-

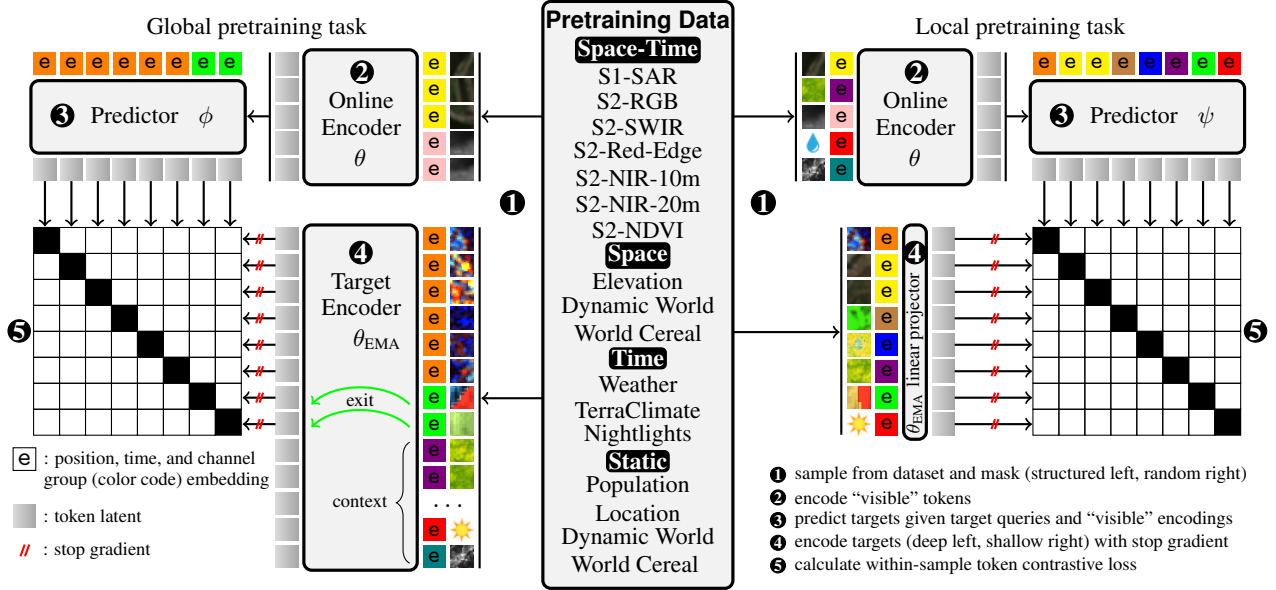


Figure 2. We train our model to learn both global and local features by alternating between the global (left) and local (right) pretraining tasks. These tasks differ in ① masking strategies and ④ target encoding strategies. In this figure, the pretraining data is split into the channel-groups described in Section 2.1.2.

ages local features, we can do better by *amplifying local details* via the PatchDisc loss. This combination amounts to performing contrastive learning in the pixel space; to our knowledge, ours is the first SSL algorithm to perform contrastive learning in the pixel space.

$$\mathcal{L}_{local} = \text{PatchDisc}(\mathbf{P}(e_2), \mathbf{E}(x_1), \text{sg}(\mathbf{E}_{EMA}^{proj}(x_2)))$$

Masking Strategy. Unstructured masking distributes the set of online and target tokens across all axes. As a result, target tokens are located close to online tokens more frequently than if contiguous masking were used. This makes local token relationships more useful to solve the pretext task. See complete masking details in Appendix A.1.2.

2.2.3. COMBINING LOCAL AND GLOBAL OBJECTIVES

While we can learn strong local and global representations independently, we aim to learn representations that excel at both. In Section 4.1, we show that these goals conflict when using a single pretraining task. Better classification hurts segmentation; better segmentation hurts classification. Combining both pretraining objectives resolves this conflict.

This combination has a secondary benefit. Latent prediction frameworks are known to be unstable; they can find trivial solutions that learn useless representations. In Section 4.1, we show that our dual objective algorithm is far more robust than single objectives.

Our dual algorithm, Galileo, alternates between global and local objectives during pretraining (Figure 2):

Table 2. Within- and between-sample token representation similarity. Measured using the cosine similarity over all EuroSat training samples.

Pretraining Objective	Within-sample Similarity	Between-sample Similarity
Global only (§2.2.1)	0.90	0.75
Local only (§2.2.2)	0.66	0.86
Combined (§2.2.3)	0.65	0.81

$$\mathcal{L}_{Galileo} = \frac{1}{2}(\mathcal{L}_{global} + \mathcal{L}_{local})$$

Ablation experiments in Section 4.1 show that PatchDisc outperforms AllDisc when combining global and local objectives, so we use PatchDisc for both objectives.

Representation measurements. We performed an experiment to verify our intuition about global and local algorithms. For all EuroSat training samples, we compute the cosine similarity between the token representations in a sample and then average across all samples, measuring the within-sample representational differences. Similarly, we average all tokens over each sample and then compute the cosine similarities between samples, measuring the between-sample differences. We find our local objective amplifies within-sample features, whereas our global objective amplifies between-sample features (Table 2). We also confirm these intuitions via downstream tasks in Section 4.1.

3. Experimental Framework

Pretraining. We pretrain three model sizes for 500 epochs using the algorithm described in Section 2.2.3. Please see the Appendix for complete details.

Downstream Tasks. We evaluate our model on all Sentinel-2 tasks in GeoBench (Lacoste et al., 2024). These cover single-timestep image classification and segmentation in various applications and geographies. We also test on fine-grained segmentation via the MADOS marine debris dataset (Kikaki et al., 2024), Sentinel-1 image segmentation via Sen1Floods11 (Bonafilia et al., 2020), image-timeseries segmentation via PASTIS (Garnot & Landrieu, 2021), optical pixel-timeseries classification via Breizhcrops (Rußwurm et al., 2019), and multimodal pixel-timeseries classification via CropHarvest (Tseng et al., 2021).

Comparisons. We benchmark our models against all SOTA pretrained RS models (described in Section 5). We report results on the full test set for each task. Feature scaling, image sizes, and hyperparameter selections have significant effects on model performance (Corley et al., 2024). We therefore rerun evaluations for all baseline models and sweep feature scaling methods and learning rates (where appropriate). In addition, we resize all images to the pretraining image size. For the image classification and segmentation tasks, we measure model results across four training set sizes (“partitions”): 100%, 20%, 5%, and 1%. We use a patch size of 4 for all models with variable patch sizes. When applying single-timestep models to the multi-timestep PASTIS dataset, we additionally sweep pooling methods to pool per-timestep encodings. See Appendix C for complete details.

4. Results

We present model rankings averaged across all tasks and partitions in Table 1. We evaluate Galileo against common RS benchmarks; however, while many pretrained models can *only* process the benchmark modalities, Galileo is trained to process numerous additional modalities which are readily available to practitioners (Table 1, “Supported Inputs”). This functionality is highly valuable to practitioners despite not being captured by these common benchmarks.

Image results. We compare Galileo to image-specialized models in Tables 3, 4 and 5; besides Satlas, these models were pretrained on single-timestep imagery, devoting all their capacity to images. Nonetheless, Galileo-Base outranks all such models on image classification and segmentation. Our lightweight models also excel at these tasks, often outperforming much larger models; we anticipate that these Galileo-Nano and Galileo-Tiny models will be highly valuable to many cost-sensitive RS practitioners in research and production. Furthermore, Galileo’s variable patch sizes allow for trade-offs between computational cost and model performance; by increasing the patch size, an instance is split up into fewer tokens, reducing the MACs required to obtain an embedding — we plot this trade-off in Figure 3.

Besides Galileo, AnySat is the only model that supports

single-timestep images and pixel-timeseries. Among these two generalist models, Galileo far exceeds AnySat on standard benchmarks, for example, by 10.8% on EuroSat.

Timeseries classification results. We compare Galileo to generalist AnySat and the pixel-timeseries specialist Presto in Table 6. We conclude similarly: Galileo outranks the specialist model and far exceeds AnySat.

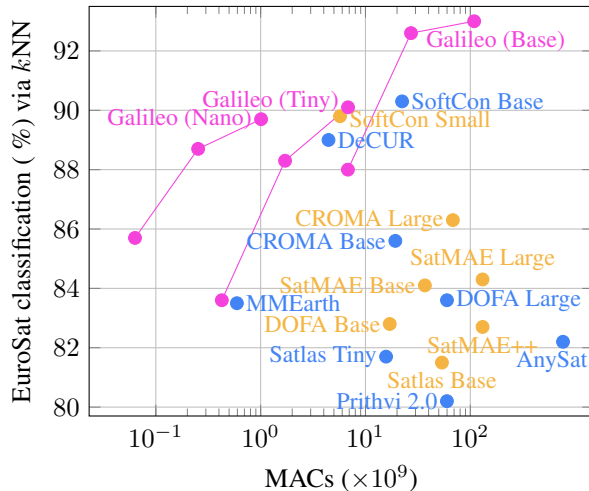


Figure 3. Practitioners can balance model performance with inference-time compute costs by varying the input patch size. This plot shows EuroSat k NN results using patch sizes $\{4, 8, 16\}$ compared with inference costs. Compute costs are measured using Multiply-Accumulate operations (MACs) required to encode a single EuroSat instance; note the log scale on the x-axis. Full results are available in Table 12.

4.1. Ablations

For all our ablation experiments, we pretrain ViT-Tiny models for 200 epochs. We select four diverse validation tasks covering segmentation (Sen1Floods11 and MADOS), image classification (EuroSat), and timeseries classification (CropHarvest), using only the validation sets for ablations.

We begin by ablating our global and local feature learning algorithms in isolation; while the global learning algorithm excels at the classification tasks and the local learning algorithm excels at the segmentation tasks, neither excel at both. We then ablate our combined algorithm, which excels on both the classification and segmentation tasks.

Ablations within our global feature learning algorithm.

We find that replacing our approach by random masking or PatchDisc significantly harms classification. Similarly our AllDisc loss outperforms MSE (used in I-JEPA) by 2.3% on EuroSat and 2.7% on CropHarvest (Tab. 7). Using only linear projections for target processing reduces performance by 2.6% on EuroSat and 2.93% on CropHarvest, confirming the importance of targeting higher-level features for classification.

Method	Arch.	m-EuroSat		m-BigEarthNet		m-So2Sat		m-Brick-Kiln	
		Training %		Training %		Training %		Training %	
		100%	1%	100%	1%	100%	1%	100%	1%
SatMAE	ViT-Base	84.1	34.8	50.6	29.0	36.0	23.1	86.1	73.5
SatMAE++	ViT-Large	82.7	48.5	50.8	31.6	34.7	23.4	89.6	76.7
CROMA	ViT-Base	85.6	<u>51.3</u>	58.8	<u>44.7</u>	48.8	33.8	92.6	85.1
SoftCon	ViT-Small	89.8	27.2	64.7	43.3	<u>51.1</u>	31.4	89.2	77.8
DOFA	ViT-Base	82.8	49.6	49.4	29.9	41.4	29.4	88.3	78.3
Satlas	Swin-Tiny	81.7	35.8	51.9	29.6	36.6	27.1	88.2	73.0
MMEarth	CNN-atto	81.7	30.0	58.3	39.6	39.8	25.1	89.4	79.7
DeCUR	ViT-Small	89.0	46.6	<u>63.8</u>	49.6	45.8	30.9	83.7	74.2
Prithvi 2.0	ViT-Large	80.2	48.0	49.4	28.8	29.5	26.1	87.9	<u>80.6</u>
AnySat	ViT-Base	82.2	47.1	54.9	33.7	39.8	29.0	85.3	72.0
Galileo	ViT-Nano	89.7	41.7	53.8	33.9	50.1	37.4	86.7	79.7
Galileo	ViT-Tiny	90.1	41.3	55.5	34.4	49.7	<u>36.2</u>	86.9	77.3
Galileo	ViT-Base	93.0	56.6	59.0	36.5	54.8	43.2	90.7	78.0

Method	Arch.	m-EuroSat		m-BigEarthNet		m-So2Sat		m-Brick-Kiln	
		Training %		Training %		Training %		Training %	
		100%	1%	100%	1%	100%	1%	100%	1%
SatMAE	ViT-Large	96.6	56.9	68.3	41.8	57.2	36.4	98.4	96.1
SatMAE++	ViT-Large	96.5	56.4	67.9	<u>45.6</u>	56.0	36.9	98.6	92.5
CROMA	ViT-Large	96.6	52.7	<u>71.9</u>	47.9	60.6	40.9	98.7	96.7
SoftCon	ViT-Base	97.5	56.3	70.3	38.5	61.7	<u>49.2</u>	98.7	97.3
DOFA	ViT-Large	96.9	53.4	68.0	43.5	58.7	37.0	98.6	94.5
Satlas	Swin-Base	97.5	51.9	72.8	25.8	<u>61.9</u>	30.6	98.4	94.7
MMEarth	CNN-atto	95.7	47.5	70.0	43.4	57.2	30.0	98.9	89.2
DeCUR	ViT-Small	97.9	54.2	70.9	44.7	61.7	47.0	98.7	96.9
Prithvi 2.0	ViT-Large	96.5	51.5	69.0	37.1	54.6	31.0	98.6	96.2
AnySat	ViT-Base	95.9	51.3	70.3	13.3	51.8	29.7	98.6	85.6
Galileo	ViT-Nano	94.5	52.6	67.1	23.3	57.4	34.9	96.1	94.2
Galileo	ViT-Tiny	96.9	<u>60.6</u>	69.7	39.5	<u>61.9</u>	43.1	98.7	96.6
Galileo	ViT-Base	<u>97.7</u>	63.5	70.7	40.9	63.3	50.6	98.7	96.8

Method	Arch.	m-Cashew-Plant		m-SA-Crop-Type		MADOS		Sen1Floods11		PASTIS	
		Training %		Training %		Training %		Training %		Training %	
		100%	1%	100%	1%	100%	1%	100%	1%	100%	1%
SatMAE	ViT-Large	30.8	22.7	24.8	16.9	55.6	13.2	N/A		29.6	11.5
SatMAE++	ViT-Large	29.6	23.3	25.7	16.8	49.9	12.7	N/A		30.5	12.0
CROMA	ViT-Base	31.8	26.8	32.0	18.3	64.2	24.4	<u>78.9</u>	77.6	<u>44.4</u>	18.5
SoftCon	ViT-Base	29.6	22.8	<u>30.8</u>	<u>18.5</u>	60.3	16.5	78.0	74.8	31.3	10.5
DOFA	ViT-Large	27.7	23.3	25.4	16.8	51.6	<u>19.1</u>	78.1	77.4	29.8	13.4
Satlas	Swin-Tiny	25.1	18.6	23.4	16.2	45.9	12.4	N/A		28.0	10.9
MMEarth	CNN-atto	24.2	20.3	22.2	14.1	34.2	16.1	N/A		24.0	10.5
DeCUR	ViT-Small	26.2	22.8	21.5	15.3	54.8	16.6	74.5	72.2	22.4	11.0
Prithvi 2.0	ViT-Large	26.7	23.2	22.9	15.7	50.0	18.9	N/A		29.3	13.2
AnySat ^a	ViT-Base	26.1	21.7	27.1	15.8	50.2	17.0	77.9	76.9	46.2	23.5
Galileo	ViT-Nano	24.4	24.5	19.7	14.5	54.8	13.9	78.6	77.1	17.5	13.1
Galileo	ViT-Tiny	27.4	<u>27.9</u>	22.5	17.1	60.8	17.5	78.0	<u>77.9</u>	28.1	16.9
Galileo	ViT-Base	<u>33.0</u>	30.2	30.1	19.4	67.6	14.7	79.4	78.2	39.2	<u>18.7</u>

^aFor semantic segmentation, AnySat outputs dense per-pixel features instead of per-patch. To keep the training-costs of the linear probes similar to other models, we sampled 6.25% of pixel features per image when training the linear probe for AnySat. Evaluation used all pixel features in an image.

Ablations within our local feature learning algorithm.

Space and time masking significantly degrade MADOS performance. Cross-batch negative sampling (AllDisc) slightly harms segmentation (Tab. 8). Using more encoder layers for target processing (as in LatentMIM’s full 12-layer approach) fails to learn useful representations, validating our targeting of low-level features through linear projections alone.

Ablations to our combined algorithm.

Leveraging PatchDisc for both objectives and providing the target encoder with all available tokens outperforms naively combining our prior global and local objectives (Tab. 9). Not sharing predictor parameters across objectives is optimal. Interestingly, our dual-objective strategy achieves successful training runs more consistently. We believe this is a

Table 3. Image classification test performance (%) via k NN. We report Top-1 accuracies for all tasks except the multilabel BigEarthNet task (for which we report F1-score). For clarity, we select the best performing model variant per baseline method, measured across all classification tasks and partitions. These model variants in some cases differ from the model variants in Table 4. Full results are available in Table 13. The the best and second best results in Table 13 are **bolded** and underlined respectively.

Table 4. Image classification test performance (%) via finetuning. We report Top-1 accuracies for all tasks except the multilabel BigEarthNet task (for which we report F1-score). For clarity, we select the best performing model variant per baseline method, measured across all classification tasks and partitions. These model variants in some cases differ from the model variants in Table 3. Full results are available in Table 14. The the best and second best results in Table 14 are **bolded** and underlined respectively.

Table 5. Image segmentation test performance (% mIoU) via linear probing. For clarity, we select the best performing model variant per baseline method, measured across all segmentation tasks and partitions. Full results are available in Table 15. The best and second best results in Table 15 are **bolded** and underlined respectively. The Sen1Floods11 dataset consists of labelling floods from SAR data; models which do not support this modality have the result replaced with N/A.

Table 6. Pixel timeseries classification performance via linear probing. The best result is **bolded** and the second best is underlined. The CropHarvest dataset contains a number of modalities in addition to Sentinel-2 optical imagery, including topography, weather and SAR data. We use all modalities each model can support.

Method	Arch.	CropHarvest			
		Togo	Brazil	Kenya	Breizhcrops
Presto	ViT-Presto	75.5	<u>98.8</u>	84.0	63.0
AnySat	ViT-Base	73.4	76.7	75.5	66.1
Galileo	ViT-Nano	73.5	76.4	<u>84.5</u>	67.3
Galileo	ViT-Tiny	74.7	<u>97.2</u>	85.4	<u>69.0</u>
Galileo	ViT-Base	<u>74.8</u>	99.3	84.2	73.0

Table 7. Ablating our *global* feature learning algorithm. MADOS and Sen1Floods11 (% mIoU) via linear probing. CropHarvest and EuroSat (% OA) via *k*NN. Our approach in **pink**. Global feature learning requires contiguous masking and abstract (deep) targets.

masking strategy	target enc. exit depth	loss function	MADOS	Floods	CropH.	EuroSat
space+time	varied	AllDisc	58.91	76.92	88.72	89.50
random	varied	AllDisc	11.71	69.62	82.12	17.40
random+space+time	varied	AllDisc	22.87	71.62	76.53	66.30
space+time	0	AllDisc	61.73	76.66	85.79	86.90
space+time	6	AllDisc	63.83	76.93	88.17	89.20
space+time	12	AllDisc	60.35	77.19	87.30	87.90
space+time	varied	MSE	62.35	76.78	86.02	87.20
space+time	varied	PatchDisc	25.74	71.68	75.30	62.50

Table 8. Ablating our *local* feature learning algorithm. MADOS and Sen1Floods11 (% mIoU) via linear probing. CropHarvest and EuroSat (% OA) via *k*NN. Our approach in **pink**. Local feature learning requires random masking and pixel (shallow) targets.

masking strategy	target enc. exit depth	loss function	MADOS	Floods	CropH.	EuroSat
random	0	PatchDisc	71.48	77.39	86.77	86.90
random+space+time	0	PatchDisc	68.63	77.82	85.31	88.80
space+time	0	PatchDisc	62.25	77.22	86.82	87.00
random	6	PatchDisc	58.53	75.66	76.58	65.40
random	12	PatchDisc	11.65	72.60	71.92	27.50
random	varied	PatchDisc	8.25	68.89	77.83	18.40
random	0	MSE	65.34	77.09	86.71	87.40
random	0	AllDisc	70.12	77.26	85.27	88.20

Table 9. Ablating our *combined* feature learning algorithm. MADOS and Sen1Floods11 (% mIoU) via linear probing. CropHarvest and EuroSat (% OA) via *k*NN. Winner in **pink**; naive combination in **gray**.

global loss	local loss	share predictors	target context	MADOS	Floods	CropH.	EuroSat
AllDisc	PatchDisc	no	dec.	63.54	76.95	86.98	89.30
PatchDisc	PatchDisc	no	all	67.79	77.66	87.87	91.00
PatchDisc	PatchDisc	no	dec.	36.98	74.21	85.49	83.30
PatchDisc	PatchDisc	no	dec.+enc.	63.41	77.36	85.87	89.30
PatchDisc	PatchDisc	yes	all	67.04	78.23	85.23	88.50
AllDisc	AllDisc	no	all	67.88	77.08	86.61	89.50
MSE	MSE	no	all	62.36	77.17	86.28	88.70

valuable finding beyond our RS focus, as improving latent prediction SSL is an active research area (Wei et al., 2024; Littwin et al., 2024; Mo & Tong, 2024).

5. Related Work and Background

Self-Supervised Learning. Reconstructing a masked or noised input is a common form of self-supervised pretraining, both for natural language (Devlin et al., 2018; Radford et al., 2018; Mikolov et al., 2013) and natural imagery (Xie et al., 2022; He et al., 2022; Vincent et al., 2008). The most successful such framework for natural imagery is masked autoencoding (MAE, He et al. (2022)), which encodes a subset of patches, then predicts the hidden patches with a decoder conditioned on the hidden patch locations. Contrastive learning (Le-Khac et al., 2020; Oord et al., 2018; Chen et al., 2020; Chopra et al., 2005) is a different approach to learning representations, which encodes samples augmented in two different ways, then attracts the representations of the same sample (called positives), and repels the representations of different samples (called negatives). Models pretrained with MAE typically outperform contrastive learning under finetuning evaluations, whereas the reverse is generally true under frozen feature evaluations (Park et al., 2023; He et al., 2022; Garrido et al., 2024).

A third paradigm has recently emerged that makes predictions in a latent space, like contrastive learning, and conditions the prediction on the sample’s transformation, like MAE. For instance, I-JEPA (Assran et al., 2023) achieves strong performance under both finetuning and frozen feature evaluations; essentially, I-JEPA modifies MAE to predict patch *representations*, computed by the encoder’s exponential moving average. LatentMIM (Wei et al., 2024) showed that I-JEPA pretraining is unstable and can be improved by their patch discrimination objective; PatchDisc attracts patch representations of the same location within an image, and repels patch representations of the same sample but different locations. Our approach falls into this third category, offering a novel learning algorithm tailored for RS.

Pretrained RS Models. SatMAE (Cong et al., 2022) adapted MAE to multispectral satellite imagery. SatMAE++ (Noman et al., 2024) improved over SatMAE by reconstructing upsampled inputs. Prithvi 2.0 (Szwarcman et al., 2024) applied MAE to Harmonized Landsat and Sentinel (HLS) multispectral imagery. CROMA (Fuller et al., 2024) adapted contrastive captioners (Yu et al., 2022) to jointly model multispectral and SAR data. SoftCon (Wang et al., 2024b) adapted supervised contrastive learning (Khosla et al., 2020; Zhang et al., 2022) to separately model multispectral and SAR data. MMEarth (Nedungadi et al., 2024) adapted convolutional MAEs (Woo et al., 2023) to reconstruct images and other RS data. Presto (Tseng et al., 2023) adapted MAE to pixel-timeseries of multispectral, SAR, and other RS data. Satlas (Bastani et al., 2023) adapted Swin transformers (Liu et al., 2021) to multispectral (and optionally multiple) images using multi-task supervised pretraining. DOFA (Xiong et al., 2024) adapted MAE to separately model multispec-

tral, SAR, and high-resolution RGB images. DeCUR (Wang et al., 2024a) adapted Barlow Twins (Zbontar et al., 2021) to separately model multispectral and SAR imagery.

While there are other pretrained models, they ingest only RGB images (Reed et al., 2023; Tang et al., 2024; Mendieta et al., 2023), have not published pretrained weights (Guo et al., 2024; Han et al., 2024), or have been surpassed by above-cited newer models (Fuller et al., 2022; Wang et al., 2023; Ayush et al., 2021; Manas et al., 2021; Jean et al., 2019; Astruc et al., 2024b; Jakubik et al., 2023).

AnySat (Astruc et al., 2024a) is concurrent with our work and shares the same spirit. It combines I-JEPA (Assran et al., 2023) and contrastive learning objectives to pretrain an RS model. AnySat is pretrained on data from more satellites, but does not include other modalities modeled by Galileo.

6. Conclusion

In this work, we identify two requirements for the application of pretrained models in a wide range of RS contexts: (i) the ability to flexibly process different modalities and input shapes, and (ii) the ability to model RS phenomena which occur at very different scales. To meet these requirements, we present the Galileo family of pretrained RS models.

We achieve these requirements by innovating on (i) the pretraining dataset used to train the Galileo models, (ii) the model architecture, allowing the model to flexibly ingest a highly multimodal dataset that varies in both space and time, and (iii) the SSL algorithm, to encourage the model to learn phenomena occurring at vastly different scales.

We run hundreds of evaluations — including extensive sweeps of baseline pretrained RS models — to robustly demonstrate Galileo’s performance across a wide range of domains, modalities, and task types. We run thorough ablations of our method. We hope the resulting insights will serve the SSL community beyond RS.

The model weights, pretraining code, pretraining data and evaluation code are open sourced at github.com/nasaharvest/galileo.

Impact Statement

Applications of machine learning to RS span a range of societally important applications, from species distribution modelling (Teng et al., 2024) to disaster management (Kansakar & Hossain, 2016). By providing a set of RS models which can perform well even when few labels are available, we hope to enable RS practitioners to continue exploring and deploying these applications. We take several steps to encourage the adoption of these models, including training the models on publicly available RS data and training a

diversity of model sizes so that they can be used in compute-constrained environments.

Tuia et al. (2023) highlight that a risk of these models is that they can be used to collect information about populations so that decisions are made without their involvement. We encourage the deployment of Galileo in collaboration with local communities and stakeholders (Krafft, 2023; Kshirsagar et al., 2021; Nakalembe & Kerner, 2023).

References

- Abatzoglou, J. T., Dobrowski, S. Z., Parks, S. A., and Hegewisch, K. C. Terraclimate, a high-resolution global dataset of monthly climate and climatic water balance from 1958–2015. *Scientific data*, 5(1):1–12, 2018.
- Assran, M., Caron, M., Misra, I., Bojanowski, P., Bordes, F., Vincent, P., Joulin, A., Rabbat, M., and Ballas, N. Masked siamese networks for label-efficient learning. In *European Conference on Computer Vision*, pp. 456–473. Springer, 2022.
- Assran, M., Duval, Q., Misra, I., Bojanowski, P., Vincent, P., Rabbat, M., LeCun, Y., and Ballas, N. Self-supervised learning from images with a joint-embedding predictive architecture. In *Proceedings of the IEEE/CVF Conference on Computer Vision and Pattern Recognition*, pp. 15619–15629, 2023.
- Astruc, G., Gonthier, N., Mallet, C., and Landrieu, L. AnySat: An Earth observation model for any resolutions, scales, and modalities. *arXiv preprint arXiv:2412.14123*, 2024a.
- Astruc, G., Gonthier, N., Mallet, C., and Landrieu, L. OmniSat: Self-supervised modality fusion for Earth observation. *ECCV*, 2024b.
- Ayush, K., Uzgent, B., Meng, C., Tanmay, K., Burke, M., Lobell, D., and Ermon, S. Geography-aware self-supervised learning. In *Proceedings of the IEEE/CVF International Conference on Computer Vision*, pp. 10181–10190, 2021.
- Baraka, S., Akera, B., Aryal, B., Sherpa, T., Shresta, F., Ortiz, A., Sankaran, K., Ferres, J. L., Matin, M., and Bengio, Y. Machine learning for glacier monitoring in the hindu kush himalaya. *arXiv preprint arXiv:2012.05013*, 2020.
- Bastani, F., Wolters, P., Gupta, R., Ferdinando, J., and Kembhavi, A. Satlaspretrain: A large-scale dataset for remote sensing image understanding. In *Proceedings of the IEEE/CVF International Conference on Computer Vision*, pp. 16772–16782, 2023.

- Beukema, P., Bastani, F., Wolters, P., Herzog, H., and Ferdinando, J. Satellite imagery and ai: A new era in ocean conservation, from research to deployment and impact. *arXiv preprint arXiv:2312.03207*, 2023.
- Beyer, L., Izmailov, P., Kolesnikov, A., Caron, M., Kornblith, S., Zhai, X., Minderer, M., Tschannen, M., Alabdulmohsin, I., and Pavetic, F. Flexivit: One model for all patch sizes. In *Proceedings of the IEEE/CVF Conference on Computer Vision and Pattern Recognition*, pp. 14496–14506, 2023.
- Bonafilia, D., Tellman, B., Anderson, T., and Issenberg, E. Sen1floods11: A georeferenced dataset to train and test deep learning flood algorithms for sentinel-1. In *Proceedings of the IEEE/CVF Conference on Computer Vision and Pattern Recognition Workshops*, pp. 210–211, 2020.
- Brown, C. F., Brumby, S. P., Guzder-Williams, B., Birch, T., Hyde, S. B., Mazzariello, J., Czerwinski, W., Pasquarella, V. J., Haertel, R., Ilyushchenko, S., et al. Dynamic world, near real-time global 10 m land use land cover mapping. *Scientific Data*, 9(1):251, 2022.
- Chen, T., Kornblith, S., Norouzi, M., and Hinton, G. A simple framework for contrastive learning of visual representations. In *International conference on machine learning*, pp. 1597–1607. PMLR, 2020.
- Chopra, S., Hadsell, R., and LeCun, Y. Learning a similarity metric discriminatively, with application to face verification. In *2005 IEEE computer society conference on computer vision and pattern recognition (CVPR'05)*, volume 1, pp. 539–546. IEEE, 2005.
- Coluzzi, R., Imbrenda, V., Lanfredi, M., and Simoniello, T. A first assessment of the sentinel-2 level 1-c cloud mask product to support informed surface analyses. *Remote sensing of environment*, 217:426–443, 2018.
- Cong, Y., Khanna, S., Meng, C., Liu, P., Rozi, E., He, Y., Burke, M., Lobell, D., and Ermon, S. Satmae: Pre-training transformers for temporal and multi-spectral satellite imagery. *Advances in Neural Information Processing Systems*, 35:197–211, 2022.
- Corley, I., Robinson, C., Dodhia, R., Ferres, J. M. L., and Najafirad, P. Revisiting pre-trained remote sensing model benchmarks: Resizing and normalization matters. In *Proceedings of the IEEE/CVF Conference on Computer Vision and Pattern Recognition (CVPR) Workshops*, pp. 3162–3172, June 2024.
- Devlin, J., Chang, M.-W., Lee, K., and Toutanova, K. Bert: Pre-training of deep bidirectional transformers for language understanding. *arXiv preprint arXiv:1810.04805*, 2018.
- Dobson, J. E., Bright, E. A., Coleman, P. R., Durfee, R. C., and Worley, B. A. Landsat: a global population database for estimating populations at risk. *Photogrammetric engineering and remote sensing*, 66(7):849–857, 2000.
- Dosovitskiy, A., Beyer, L., Kolesnikov, A., Weissenborn, D., Zhai, X., Unterthiner, T., Dehghani, M., Minderer, M., Heigold, G., Gelly, S., Uszkoreit, J., and Houselby, N. An image is worth 16x16 words: Transformers for image recognition at scale. In *International Conference on Learning Representations*, 2021. URL <https://openreview.net/forum?id=YicbFdNTTy>.
- Elvidge, C. D., Baugh, K., Zhizhin, M., Hsu, F. C., and Ghosh, T. Viirs night-time lights. *International journal of remote sensing*, 38(21):5860–5879, 2017.
- ESA. Mission ends for copernicus sentinel-1b satellite. https://www.esa.int/Applications/Observing_the_Earth/Copernicus/Sentinel-1/Mission_ends_for_Copernicus_Sentinel-1B_satellite, 2023.
- Frame, J. M., Nair, T., Sunkara, V., Popien, P., Chakrabarti, S., Anderson, T., Leach, N. R., Doyle, C., Thomas, M., and Tellman, B. Rapid inundation mapping using the us national water model, satellite observations, and a convolutional neural network. *Geophysical Research Letters*, 51(17):e2024GL109424, 2024.
- Fuller, A., Millard, K., and Green, J. R. SatViT: Pretraining transformers for earth observation. *IEEE Geoscience and Remote Sensing Letters*, 19:1–5, 2022.
- Fuller, A., Millard, K., and Green, J. CROMA: Remote sensing representations with contrastive radar-optical masked autoencoders. *Advances in Neural Information Processing Systems*, 36, 2024.
- Garnot, V. S. F. and Landrieu, L. Panoptic segmentation of satellite image time series with convolutional temporal attention networks. In *Proceedings of the IEEE/CVF International Conference on Computer Vision*, pp. 4872–4881, 2021.
- Garrido, Q., Assran, M., Ballas, N., Bardes, A., Najman, L., and LeCun, Y. Learning and leveraging world models in visual representation learning. *arXiv preprint arXiv:2403.00504*, 2024.
- Gorelick, N., Hancher, M., Dixon, M., Ilyushchenko, S., Thau, D., and Moore, R. Google earth engine: Planetary-scale geospatial analysis for everyone. *Remote sensing of Environment*, 202:18–27, 2017.

- Guo, X., Lao, J., Dang, B., Zhang, Y., Yu, L., Ru, L., Zhong, L., Huang, Z., Wu, K., Hu, D., et al. Skysense: A multi-modal remote sensing foundation model towards universal interpretation for earth observation imagery. In *Proceedings of the IEEE/CVF Conference on Computer Vision and Pattern Recognition*, pp. 27672–27683, 2024.
- Gwilliam, M. and Shrivastava, A. Beyond supervised vs. unsupervised: Representative benchmarking and analysis of image representation learning. In *Proceedings of the IEEE/CVF Conference on Computer Vision and Pattern Recognition*, pp. 9642–9652, 2022.
- Han, B., Zhang, S., Shi, X., and Reichstein, M. Bridging remote sensors with multisensor geospatial foundation models. In *Proceedings of the IEEE/CVF Conference on Computer Vision and Pattern Recognition*, pp. 27852–27862, 2024.
- He, K., Chen, X., Xie, S., Li, Y., Dollár, P., and Girshick, R. Masked autoencoders are scalable vision learners. In *Proceedings of the IEEE/CVF conference on computer vision and pattern recognition*, pp. 16000–16009, 2022.
- Helber, P., Bischke, B., Dengel, A., and Borth, D. Eurosat: A novel dataset and deep learning benchmark for land use and land cover classification. *IEEE Journal of Selected Topics in Applied Earth Observations and Remote Sensing*, 12(7):2217–2226, 2019.
- Hersbach, H., Bell, B., Berrisford, P., Hirahara, S., Horányi, A., Muñoz-Sabater, J., Nicolas, J., Peubey, C., Radu, R., Schepers, D., et al. The era5 global reanalysis. *Quarterly Journal of the Royal Meteorological Society*, 146(730): 1999–2049, 2020.
- Hoffer, E., Ben-Nun, T., Hubara, I., Giladi, N., Hoefler, T., and Soudry, D. Augment your batch: better training with larger batches. *arXiv preprint arXiv:1901.09335*, 2019.
- Jakubik, J., Roy, S., Phillips, C., Fraccaro, P., Godwin, D., Zadrozny, B., Szwarcman, D., Gomes, C., Nyirjesy, G., Edwards, B., et al. Foundation models for generalist geospatial artificial intelligence. *CoRR*, 2023.
- Jean, N., Wang, S., Samar, A., Azzari, G., Lobell, D., and Ermon, S. Tile2vec: Unsupervised representation learning for spatially distributed data. In *Proceedings of the AAAI Conference on Artificial Intelligence*, pp. 3967–3974, 2019.
- Kansakar, P. and Hossain, F. A review of applications of satellite earth observation data for global societal benefit and stewardship of planet earth. *Space Policy*, 2016.
- Kebede, E. A., Abou Ali, H., Clavelle, T., Froehlich, H. E., Gephart, J. A., Hartman, S., Herrero, M., Kerner, H., Mehta, P., Nakalembe, C., et al. Assessing and addressing the global state of food production data scarcity. *Nature Reviews Earth & Environment*, 5(4):295–311, 2024.
- Kerner, H., Tseng, G., Becker-Reshef, I., Nakalembe, C., Barker, B., Munshell, B., Paliyam, M., and Hosseini, M. Rapid response crop maps in data sparse regions. In *ACM SIGKDD Conference on Data Mining and Knowledge Discovery Workshops*, 2020.
- Khosla, P., Teterwak, P., Wang, C., Sarna, A., Tian, Y., Isola, P., Maschinot, A., Liu, C., and Krishnan, D. Supervised contrastive learning. *Advances in neural information processing systems*, 33:18661–18673, 2020.
- Kikaki, K., Kakogeorgiou, I., Hoteit, I., and Karantzalos, K. Detecting marine pollutants and sea surface features with deep learning in sentinel-2 imagery. *ISPRS Journal of Photogrammetry and Remote Sensing*, 210:39–54, 2024.
- Krafft, A. ASU researcher combats food insecurity with AI. <https://news.asu.edu/20230303-solutions-asu-researcher-combats-food-insecurity-ai>, 2023. Accessed: 2023-09-21.
- Kruse, C., Boyda, E., Chen, S., Karra, K., Bou-Nahra, T., Hammer, D., Mathis, J., Maddalene, T., Jambeck, J., and Laurier, F. Satellite monitoring of terrestrial plastic waste. *PloS one*, 18(1):e0278997, 2023.
- Kshirsagar, M., Robinson, C., Yang, S., Gholami, S., Klyuzhin, I., Mukherjee, S., Nasir, M., Ortiz, A., Oviedo, F., Tanner, D., et al. Becoming good at ai for good. In *AAAI/ACM Conference on AI, Ethics, and Society*, 2021.
- Lacoste, A., Lehmann, N., Rodriguez, P., Sherwin, E., Kerner, H., Lütjens, B., Irvin, J., Dao, D., Alemohammad, H., Drouin, A., et al. Geo-bench: Toward foundation models for earth monitoring. *Advances in Neural Information Processing Systems*, 36, 2024.
- Le-Khac, P. H., Healy, G., and Smeaton, A. F. Contrastive representation learning: A framework and review. *Ieee Access*, 8:193907–193934, 2020.
- Lee, J., Brooks, N. R., Tajwar, F., Burke, M., Ermon, S., Lobell, D. B., Biswas, D., and Luby, S. P. Scalable deep learning to identify brick kilns and aid regulatory capacity. *Proceedings of the National Academy of Sciences*, 118(17):e2018863118, 2021.
- Littwin, E., Thilak, V., and Gopalakrishnan, A. Enhancing jepas with spatial conditioning: Robust and efficient representation learning, 2024. URL <https://arxiv.org/abs/2410.10773>.
- Liu, Z., Lin, Y., Cao, Y., Hu, H., Wei, Y., Zhang, Z., Lin, S., and Guo, B. Swin transformer: Hierarchical vision transformer using shifted windows. In *Proceedings of the*

- IEEE/CVF international conference on computer vision*, pp. 10012–10022, 2021.
- Manas, O., Lacoste, A., Giró-i Nieto, X., Vazquez, D., and Rodriguez, P. Seasonal contrast: Unsupervised pre-training from uncurated remote sensing data. In *Proceedings of the IEEE/CVF International Conference on Computer Vision*, pp. 9414–9423, 2021.
- Mendieta, M., Han, B., Shi, X., Zhu, Y., and Chen, C. Towards geospatial foundation models via continual pre-training. In *Proceedings of the IEEE/CVF International Conference on Computer Vision*, pp. 16806–16816, 2023.
- Mikolov, T., Chen, K., Corrado, G., and Dean, J. Efficient estimation of word representations in vector space, 2013. URL <https://arxiv.org/abs/1301.3781>.
- Mo, S. and Tong, S. Connecting joint-embedding predictive architecture with contrastive self-supervised learning. In *The Thirty-eighth Annual Conference on Neural Information Processing Systems*, 2024. URL <https://openreview.net/forum?id=JvQnJWIj6m>.
- Nakalembe, C. and Kerner, H. Considerations for ai-eeo for agriculture in sub-saharan africa. *Environmental Research Letters*, 2023.
- NASA JPL. NASA shuttle radar topography mission global 1 arc second. NASA EOSDIS Land Processes Distributed Active Archive Center, 2000.
- Nedungadi, V., Kariryaa, A., Oehmcke, S., Belongie, S., Igel, C., and Lang, N. Mmearth: Exploring multi-modal pretext tasks for geospatial representation learning, 2024.
- Noman, M., Naseer, M., Cholakkal, H., Anwer, R. M., Khan, S., and Khan, F. S. Rethinking transformers pre-training for multi-spectral satellite imagery. In *Proceedings of the IEEE/CVF Conference on Computer Vision and Pattern Recognition*, pp. 27811–27819, 2024.
- Oord, A. v. d., Li, Y., and Vinyals, O. Representation learning with contrastive predictive coding. *arXiv preprint arXiv:1807.03748*, 2018.
- Park, N., Kim, W., Heo, B., Kim, T., and Yun, S. What do self-supervised vision transformers learn? In *The Eleventh International Conference on Learning Representations*, 2023. URL <https://openreview.net/forum?id=azCKuYs74>.
- Pedregosa, F., Varoquaux, G., Gramfort, A., Michel, V., Thirion, B., Grisel, O., Blondel, M., Prettenhofer, P., Weiss, R., Dubourg, V., et al. Scikit-learn: Machine learning in python. *the Journal of machine Learning research*, 12:2825–2830, 2011.
- Poggio, L., De Sousa, L. M., Batjes, N. H., Heuvelink, G. B., Kempen, B., Ribeiro, E., and Rossiter, D. Soilgrids 2.0: producing soil information for the globe with quantified spatial uncertainty. *Soil*, 7(1):217–240, 2021.
- Radford, A., Narasimhan, K., Salimans, T., and Sutskever, I. Improving language understanding by generative pre-training. *OpenAI technical reports*, 2018.
- Reed, C. J., Gupta, R., Li, S., Brockman, S., Funk, C., Clipp, B., Keutzer, K., Candido, S., Uyttendaele, M., and Darrell, T. Scale-mae: A scale-aware masked autoencoder for multiscale geospatial representation learning. In *Proceedings of the IEEE/CVF International Conference on Computer Vision*, pp. 4088–4099, 2023.
- Rußwurm, M., Lefèvre, S., and Körner, M. Breizhcrops: A satellite time series dataset for crop type identification. In *Proceedings of the International Conference on Machine Learning Time Series Workshop*, volume 3, 2019.
- Sumbul, G., Charfuelan, M., Demir, B., and Markl, V. Bigearthnet: A large-scale benchmark archive for remote sensing image understanding. In *IGARSS 2019-2019 IEEE International Geoscience and Remote Sensing Symposium*, pp. 5901–5904. IEEE, 2019.
- Szwarcman, D., Roy, S., Fraccaro, P., Gíslason, T. E., Blumenstiel, B., Ghosal, R., de Oliveira, P. H., Almeida, J. L. d. S., Sedona, R., Kang, Y., et al. Prithvi-eeo-2.0: A versatile multi-temporal foundation model for earth observation applications. *arXiv preprint arXiv:2412.02732*, 2024.
- Tang, M., Cozma, A., Georgiou, K., and Qi, H. Cross-scale mae: A tale of multiscale exploitation in remote sensing. *Advances in Neural Information Processing Systems*, 36, 2024.
- Teng, M., Elmustafa, A., Akera, B., Bengio, Y., Radi, H., Larochelle, H., and Rolnick, D. Satbird: a dataset for bird species distribution modeling using remote sensing and citizen science data. *Advances in Neural Information Processing Systems*, 36, 2024.
- Tseng, G., Zvonkov, I., Nakalembe, C. L., and Kerner, H. Cropharvest: A global dataset for crop-type classification. In *Thirty-fifth Conference on Neural Information Processing Systems Datasets and Benchmarks Track (Round 2)*, 2021.
- Tseng, G., Cartuyvels, R., Zvonkov, I., Purohit, M., Rolnick, D., and Kerner, H. Lightweight, pre-trained transformers for remote sensing timeseries. *arXiv preprint arXiv:2304.14065*, 2023.
- Tucker, C. J. Red and photographic infrared linear combinations for monitoring vegetation. *Remote sensing of Environment*, 8(2):127–150, 1979.

- Tuia, D., Schindler, K., Demir, B., Camps-Valls, G., Zhu, X. X., Kochupillai, M., Džeroski, S., van Rijn, J. N., Hoos, H. H., Del Frate, F., et al. Artificial intelligence to advance earth observation: a perspective. *arXiv preprint arXiv:2305.08413*, 2023.
- Uber. H3: A hexagonal hierarchical geospatial indexing system. <https://h3geo.org>, 2018. Accessed: 2024-12-04.
- Van Tricht, K., Degerickx, J., Gilliams, S., Zanaga, D., Battude, M., Grosu, A., Brombacher, J., Lesiv, M., Bayas, J. C. L., Karanam, S., et al. Worldcereal: a dynamic open-source system for global-scale, seasonal, and reproducible crop and irrigation mapping. *Earth System Science Data Discussions*, 2023:1–36, 2023.
- Vincent, P., Larochelle, H., Bengio, Y., and Manzagol, P.-A. Extracting and composing robust features with denoising autoencoders. In *Proceedings of the 25th international conference on Machine learning*, pp. 1096–1103, 2008.
- Wang, Y., Braham, N. A. A., Xiong, Z., Liu, C., Albrecht, C. M., and Zhu, X. X. SSL4EO-S12: A large-scale multimodal, multitemporal dataset for self-supervised learning in Earth observation. *IEEE Geoscience and Remote Sensing Magazine*, 11(3):98–106, 2023.
- Wang, Y., Albrecht, C. M., Braham, N. A. A., Liu, C., Xiong, Z., and Zhu, X. X. Decoupling common and unique representations for multimodal self-supervised learning. *arXiv preprint arXiv:2309.05300*, 2024a.
- Wang, Y., Albrecht, C. M., and Zhu, X. X. Multi-Label Guided Soft Contrastive Learning for Efficient Earth Observation Pretraining. *arXiv preprint arXiv:2405.20462*, 2024b.
- Wei, Y., Gupta, A., and Morgado, P. Towards latent masked image modeling for self-supervised visual representation learning. In *ECCV*, 2024.
- Woo, S., Debnath, S., Hu, R., Chen, X., Liu, Z., Kweon, I. S., and Xie, S. Convnext v2: Co-designing and scaling convnets with masked autoencoders. In *Proceedings of the IEEE/CVF Conference on Computer Vision and Pattern Recognition*, pp. 16133–16142, 2023.
- Xie, Z., Zhang, Z., Cao, Y., Lin, Y., Bao, J., Yao, Z., Dai, Q., and Hu, H. Simmim: A simple framework for masked image modeling. In *Proceedings of the IEEE/CVF conference on computer vision and pattern recognition*, pp. 9653–9663, 2022.
- Xiong, Z., Wang, Y., Zhang, F., Stewart, A. J., Hanna, J., Borth, D., Papoutsis, I., Saux, B. L., Camps-Valls, G., and Zhu, X. X. Neural plasticity-inspired foundation model for observing the earth crossing modalities. *arXiv preprint arXiv:2403.15356*, 2024.
- Yin, L., Ghosh, R., Lin, C., Hale, D., Weigl, C., Obarowski, J., Zhou, J., Till, J., Jia, X., You, N., et al. Mapping smallholder cashew plantations to inform sustainable tree crop expansion in benin. *Remote Sensing of Environment*, 295:113695, 2023.
- Yu, J., Wang, Z., Vasudevan, V., Yeung, L., Seyedhosseini, M., and Wu, Y. Coca: Contrastive captioners are image-text foundation models. *Transactions on Machine Learning Research*, 2022. ISSN 2835-8856. URL <https://openreview.net/forum?id=Ee277P3AYC>.
- Zanaga, D., Van De Kerchove, R., Daems, D., De Keersmaecker, W., Brockmann, C., Kirches, G., Wevers, J., Cartus, O., Santoro, M., Fritz, S., et al. Esa worldcover 10 m 2021 v200. *ESA WorldCover Project*, 2022.
- Zbontar, J., Jing, L., Misra, I., LeCun, Y., and Deny, S. Barlow twins: Self-supervised learning via redundancy reduction. In *International conference on machine learning*, pp. 12310–12320. PMLR, 2021.
- Zhang, S., Xu, R., Xiong, C., and Ramaiah, C. Use all the labels: A hierarchical multi-label contrastive learning framework. In *Proceedings of the IEEE/CVF Conference on Computer Vision and Pattern Recognition*, pp. 16660–16669, 2022.
- Zhu, X. X., Hu, J., Qiu, C., Shi, Y., Kang, J., Mou, L., Bagheri, H., Haberle, M., Hua, Y., Huang, R., et al. So2sat lc42: A benchmark data set for the classification of global local climate zones [software and data sets]. *IEEE Geoscience and Remote Sensing Magazine*, 8(3): 76–89, 2020.

A. Methodology details

A.1. The Galileo SSL algorithm

We adopt a latent prediction framework inspired by Assran et al. (2023), Garrido et al. (2024), and Wei et al. (2024), which operates as follows: **1** Given a batch of samples, we construct two *different* views of each sample, $\mathbf{x}_1 \in \mathbb{R}^{L_1 \times D}$ and $\mathbf{x}_2 \in \mathbb{R}^{L_2 \times D}$. **2** Our “online” encoder computes patch encodings $\mathbf{z}_1 = \mathbf{E}(\mathbf{x}_1)$, while our “target” encoder — an exponential moving average of the online encoder — computes target patch encodings $\mathbf{z}_2 = \mathbf{E}_{\text{EMA}}(\mathbf{x}_2)$. **3** A predictor transformer \mathbf{P} receives the target view’s position, time, month, and channel group embeddings $\mathbf{e}_2 \in \mathbb{R}^{L_2 \times D}$ as placeholder queries and predicts patch encodings $\mathbf{p} \in \mathbb{R}^{L_2 \times D}$ by cross-attending to the online patch encodings, i.e., $\mathbf{p} = \mathbf{P}(\mathbf{e}_2, \mathbf{z}_1)$. **4** The predictions \mathbf{p} and targets \mathbf{z}_2 are compared to compute a loss $\mathcal{L}(\mathbf{p}, \mathbf{z}_2)$ that updates the online encoder.

We adapt this latent prediction framework for learning local and global features. We outline those adaptations below.

A.1.1. LEARNING GLOBAL FEATURES

We design this algorithm to learn abstract, lower-frequency features suited for classification applications. **1** View construction involves: **a** uniformly sampling the number of channel groups $N \in \{2, 3, \dots, 17\}$, **b** randomly selecting N channel groups (e.g., RGB, SAR, ERA5), **c** repeating steps (a-b) for the target encoder while excluding overlapping channel groups, **d** applying either spatial or temporal masking, and **e** tokenizing both views to obtain \mathbf{x}_1 and \mathbf{x}_2 . Space masking samples masks across space while maintaining consistency across channel groups and time; time masking does the same across time while maintaining consistency across channel groups and space. **2–3** Following our general framework, we compute \mathbf{z}_1 and \mathbf{p} , and compute targets using varied exit depths from the target encoder, $\mathbf{E}_{\text{EMA}}^\ell$. **4** We use our AllDisc loss (defined in Section 2.2.1) as:

$$\mathcal{L}_{\text{global}} = \text{AllDisc}(\mathbf{P}(\mathbf{e}_2, \mathbf{E}(\mathbf{x}_1)), \text{sg}(\mathbf{E}_{\text{EMA}}^\ell(\mathbf{x}_2)))$$

A.1.2. LEARNING LOCAL FEATURES

We design this algorithm to learn fine-grained, higher-frequency features suited for segmentation applications. **1** View construction involves: **a** tokenizing the entire sample, and **b** randomly selecting 5% of tokens for \mathbf{x}_1 and 50% for \mathbf{x}_2 . **2–3** Following our general framework, we compute \mathbf{z}_1 and \mathbf{p} , but compute targets using only the target encoder’s linear projection, i.e., $\mathbf{E}_{\text{EMA}}^{\text{proj}}$ — skipping transformer blocks such that the predictor targets low-level features. **4** We use LatentMIM’s PatchDisc loss, tasking the model to discriminate between patches on the basis of low-level features alone:

$$\mathcal{L}_{\text{local}} = \text{PatchDisc}(\mathbf{P}(\mathbf{e}_2, \mathbf{E}(\mathbf{x}_1)), \text{sg}(\mathbf{E}_{\text{EMA}}^{\text{proj}}(\mathbf{x}_2)))$$

A.1.3. COMBINING LOCAL AND GLOBAL OBJECTIVES

As noted in Section 2.2.3, our combined method alternates between the local and global objectives during pretraining:

$$\mathcal{L}_{\text{Galileo}} = \frac{1}{2}(\mathcal{L}_{\text{global}} + \mathcal{L}_{\text{local}})$$

B. Pretraining details

B.1. A globally sampled pretraining dataset

To construct the Galileo dataset, we split the global WorldCover map (Zanaga et al., 2022) into 1000×1000 pixels ($10\text{km} \times 10\text{km}$) tiles. For each tile, we compute two feature sets: **1** the number of pixels within each WorldCereal classification class, and **2** the latitude and longitude of the tile. We use these features to train a $k=150,000$ k -means clustering algorithm, and select the tiles closest to the centroid of each cluster. This yields 150,000 training points, of which 85% (127,155) are successfully exported using Google Earth Engine (Gorelick et al., 2017). By including both the pixel counts and the latitude and longitudes as features to the k -means algorithm, we ensure both the semantic and geographic diversity of the model’s training points — Figure 4 shows a choropleth map of the exported points.

We use this sampling procedure to construct a rich dataset to pretrain our model. This dataset consists of 9 RS inputs, ranging from directly sensed inputs (such as Sentinel-2 optical imagery) to semantically dense maps (such as the Dynamic World landcover maps) — these are discussed in detail in Section 2.1.1. Table 10 studies the impact of each of these modalities on the model’s downstream performance, by pretraining the global-local model (Section 2.2.3) while omitting a single data

product.

Table 10. Ablating the Galileo dataset. MADOS and Sen1Floods11 (% mIoU) via linear probing. CropHarvest and EuroSat (% OA) via k NN.

Removed input	MADOS	Sen1Floods11	CropHarvest	EuroSat
None	67.79	77.66	87.87	91.00
S1	67.67	N/A	85.27	90.20
NDVI	67.89	78.10	88.32	90.00
ERA5	68.10	77.10	87.14	91.20
TerraClim	61.30	74.90	82.78	81.20
VIIRS	63.48	74.52	84.10	81.10
SRTM	66.14	77.62	86.74	91.00
DynamicWorld	67.24	77.86	87.80	89.30
WorldCereal	65.94	77.56	87.71	89.60
LandScan	60.74	77.45	87.89	91.10

B.2. Implementation

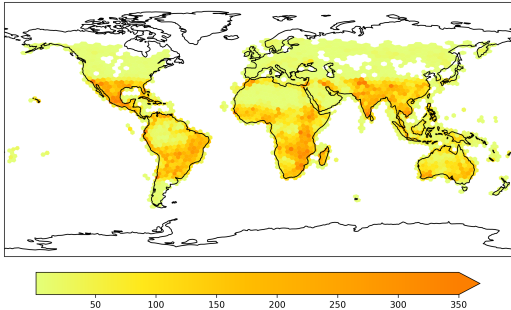


Figure 4. The number of exported training points per H3 cell (Uber, 2018) at resolution = 2. We sample from the entire globe, aiming for semantic diversity (defined by the WorldCover landcover map classes (Zanaga et al., 2022)) and geographic coverage.

All models are trained on single H100 GPUs (model sizes and training times are described in Table 11). We use an effective batch size of 512, which consists of a minibatches of 128 instances augmented and repeated 4 times (Hoffer et al., 2019). For data augmentations, we randomly apply vertical and horizontal flipping and 90-degree rotations to each instance. When repeating the data, we first randomly select a patch size $P \in [1, 2, 3, 4, 5, 6, 7, 8]$. We then randomly select a (size, timestep) combination $(S, T) \in [(4, 12), (5, 6), (6, 4), (7, 3), (9, 3), (12, 3)]$. We then randomly subset spatially height $H = P \times S$, width $W = P \times S$ and timesteps T from each instance in the batch.

We use bfloat16 precision, and the AdamW optimizer with $\beta_1 = 0.9$ and $\beta_2 = 0.999$ with gradient clipping. We warmup our learning rate for 30 epochs to a maximum learning rate before applying a cooldown via a cosine decay schedule. We use exponential moving averaging (EMA) to update our target encoder with a momentum value of 0.996 which linearly increases to 1 throughout pretraining following Assran et al. (2022).

For all ablations (Section 4.1), we pretrain a ViT-Tiny model for 200 epochs to a maximum learning rate of 2×10^{-3} and use a weight decay of 0.02. For the final Galileo models, we pretrain the models for 500 epochs and conduct a sweep of [learning rate \times weight decay]. For the ViT-Nano and ViT-Tiny architectures, we sweep learning rates $\in [1 \times 10^{-3}, 2 \times 10^{-3}, 3 \times 10^{-3}]$ and weight decays $\in [1 \times 10^{-2}, 2 \times 10^{-2}, 3 \times 10^{-2}]$. For the ViT-Base architecture, we sweep learning rates $\in [1 \times 10^{-4}, 3 \times 10^{-4}, 1 \times 10^{-3}, 2 \times 10^{-3}, 3 \times 10^{-3}]$ and weight decays $\in [1 \times 10^{-2}, 2 \times 10^{-2}, 3 \times 10^{-2}]$.

C. Evaluation details

C.1. Implementation

To ensure consistent experimental settings when comparing pretrained models, we rerun all evaluations under identical conditions. For the k NN probing, we follow the implementation of Gwilliam & Shrivastava (2022) — we use the pretrained models to compute representations of the test data (as values) and training data (as keys) — we then use the keys to classify the test data. Following Fuller et al. (2024) and Reed et al. (2023), we use $k = 20$. When linear probing, we use the pretrained models to compute representations of the training data and use this to train linear probes. We sweep learning rates when training the linear probes ($\{1, 3, 4, 5\} \times 10^{\{-4, -3, -2, -1\}}$) and apply the trained linear probes to the computed representations of the test data. When finetuning, we sweep learning rates when finetuning ($\{1, 3, 6\} \times 10^{\{-5, -4, -3\}}$) and apply the finetuned models to the test data.

Table 11. Configurations of our ViT models and associated pretraining costs. GPU-hours describes the number of GPU-hours required to pretrain each model for 500 epochs on an H100 GPU.

architecture	blocks	dim	heads	params	GPU-hours
ViT-Nano	4	128	8	0.8M	200
ViT-Tiny	12	192	3	5.3M	259
ViT-Base	12	768	12	85.0M	573

C.2. Evaluation Datasets

We evaluate our models on the datasets described below. For all GeoBench-modified datasets (Lacoste et al., 2024) - m-Eurosat, m-BigEarthnet, m-So2Sat, m-Brick-Kiln, m-Cashew-Plant and m-SA-Crop-Type, we use the training, validation and test splits shared by GeoBench. In addition, we use the 1%, 5% and 20% partitions shared by GeoBench.

- **m-EuroSat** (Helber et al., 2019): The full training set consists of 2,000 images, with 1,000 images in the validation and test sets. Images are 64×64 pixels.
- **m-BigEarthNet** (Sumbul et al., 2019): The full training set consists of 20,000 images, with 1,000 images in the test set. Images are 120×120 pixels.
- **m-So2Sat** (Zhu et al., 2020): The full training set consists of 19,992 images (with 986 images in the test set), and images are 32×32 pixels.
- **m-Brick-Kiln** (Lee et al., 2021): The full training set consists of 15,063 images, with 999 images in the test set. Images are 64×64 pixels.
- **m-Cashew-Plant** (Yin et al., 2023): The full training set consists of 1,350 images, with 50 images in the test set. Images are 256×256 ; we subtile them into 64×64 images.
- **m-SA-crop-type** (link): The full training set consists of 3,000 images, with 93 images in the test set. Images are 256×256 ; we subtile them into 64×64 images.
- **MADOS** (Kikaki et al., 2024): The full MADOS dataset consists of 2,804 140×140 images, extracted from 174 Sentinel-2 scenes. We use the train/val/test splits from MADOS (50%/25%/25%) — each split was created as a representative subset of the entire MADOS dataset. In addition, we subtile each image into 80×80 images.
- **PASTIS** (Garnot & Landrieu, 2021): The full PASTIS dataset consists of 2,433 128×128 timeseries, with 38-61 timesteps per timeseries. We subtile each timeseries spatially into 64×64 images. In addition, we compute monthly aggregations of the timeseries. Garnot & Landrieu (2021) share 5 folds of the data; we use folds $\{1, 2, 3\}$ for training, 4 for validation and 5 for testing. When applying single-timestep models to this dataset, we additionally sweep pooling methods to pool per-timestep encodings (as described in Section C).
- **Breizhcrops** (Rußwurm et al., 2019): The Breizhcrops dataset consists of pixel-timeseries in 4 NUTS-3 regions in Brittany, France. We use 2 for training (FRH01, with 178,613 parcels and FRH02 with 140,645 parcels). We use FRH03 (166,391 parcels) for validation and FRH04 (122,614 parcels) for testing. The dataset consists of variable sequence lengths; we compute monthly aggregations of the timeseries.
- **CropHarvest** (Tseng et al., 2021): The CropHarvest dataset consists of 3 pixel-timeseries tasks: (i) crop vs. non crop in Togo, with 1,319 samples in the training set and 306 samples in the test set, (ii) maize vs. rest in Kenya with 1,345 samples in the training set and 1,942 m^2 of densely labelled pixels in the test set, and (iii) coffee vs. rest in Brazil with 794 samples in the training set and 4.2 km^2 of densely labelled pixels in the test set.

C.3. Comparing to baseline models

Corley et al. (2024) found that input-image sizes and feature scaling methods can have significant impacts on the performance of pretrained RS models. We therefore resize all input images to the sizes that the models were pretrained on. In addition, we treat feature scaling methods as an additional hyperparameter, and sweep it in addition to the learning rates (where those are applicable, i.e. for linear probing and finetuning). Finally, the PASTIS dataset consists of multiple timesteps of optical imagery. Since all benchmark models (except AnySat) cannot ingest the full timeseries natively, we use multiple forward

passes. We select two methods for combining the outputs of these forward passes - ❶ a mean of the encodings, and ❷ a max, following Bastani et al. (2023).

The reported test results are therefore computed by sweeping the cross product of the following hyperparameters:

$$[\text{Learning Rate}] \times [\text{Temporal aggregations}]$$

We select all hyperparameters using the validation sets in the downstream datasets.

In addition to conducting this sweep, we run the linear probes 5 times and average the results. When running the linear probe, we sweep the learning rate and feature scaling method concurrently for the first run. We select the feature scaling method from this first run, and fix it for all subsequent runs. We then select the best other hyperparameters per run, and aggregate these to obtain our final results.

We run this sweep for all evaluation datasets with the exception of the CropHarvest tasks; these consist of small training sets and no validation sets against which the hyperparameters can be selected. We therefore follow Tseng et al. (2023) in using the same feature scaling methods as was used during pretraining, and using scikit-learn’s regression algorithm with default parameters (Pedregosa et al., 2011) for all models.

C.3.1. FEATURE SCALING

The pretrained models we benchmark against apply either standardization (MMEarth, DOFA, AnySat and Presto) or normalization (all other models) during pretraining. We sweep the following normalization statistics, either via standardization or normalization depending on the pre-training procedure: ❶ statistics from the downstream datasets, ❷ SatMAE pretraining statistics, ❸ SSL4EO (Wang et al., 2023) statistics, ❹ Galileo pretraining dataset statistics, ❺ Presto pretraining dataset statistics. For all of these statistics, we additionally sweep standard deviation multipliers. Prithvi 2.0 statistics only cover a subset of Sentinel-2 bands; we therefore only include those statistics in the sweeps for the Prithvi 2.0 model.

D. Results

We include full results for the image classification tasks (Table 13) and segmentation tasks (Table 15). In addition, full results for the m-Eurosat dataset with varying patch sizes are recorded in Table 12 - these values are used in Figure 3.

We rank the models in Table 16. When ranking the models, we compute the average rank of each model across each dataset and partition.

Table 12. Galileo m-Eurosat classification test performance (%) as a function of patch size measured via k NN for different training set %s. MACs required to process a single EuroSat instance are also recorded; by selecting the model size and patch size, practitioners can make trade offs between model performance and inference costs.

Arch.	patch size	GMACs	100 %	20 %	5%	1%
ViT-Nano	8	0.25	88.7	81.9	55.0	38.5
	16	0.06	85.7	79.3	56.0	41.1
ViT-Tiny	8	1.71	88.3	83.0	59.7	41.3
	16	0.43	83.6	78.4	50.1	33.8
ViT-Base	8	27.20	92.6	88.3	72.4	56.9
	16	6.80	88.0	82.4	58.6	48.9

Table 13. Image classification test performance (%) via k NN. Ranks are calculated by averaging all results and ranking the averages.

Method	Arch.	m-EuroSat				m-BigEarthNet				m-So2Sat				m-Brick-Kiln			
		Training %, Top-1 Acc. \uparrow				Training %, F1 Score \uparrow				Training %, Top-1 Acc. \uparrow				Training %, Top-1 Acc. \uparrow			
		100%	20%	5%	1%	100%	20%	5%	1%	100%	20%	5%	1%	100%	20%	5%	1%
SatMAE (Cong et al., 2022)	ViT-Base	84.1	73.3	50.1	34.8	50.6	42.5	35.7	29.0	36.0	32.9	29.7	23.1	86.1	81.9	80.3	73.5
SatMAE (Cong et al., 2022)	ViT-Large	84.3	74.7	53.1	46.4	50.8	42.9	35.6	27.7	36.6	34.3	31.0	24.4	87.9	84.0	80.4	74.7
SatMAE++ (Noman et al., 2024)	ViT-Large	82.7	75.9	51.1	48.5	50.8	42.8	36.7	31.6	34.7	32.7	29.9	23.4	89.6	87.1	82.8	76.7
CROMA (Fuller et al., 2024)	ViT-Base	85.6	79.4	66.2	<u>51.3</u>	58.8	55.3	49.3	<u>44.7</u>	48.8	48.0	43.9	33.8	92.6	90.6	87.7	85.1
CROMA (Fuller et al., 2024)	ViT-Large	86.3	78.1	59.9	49.0	56.6	50.6	44.1	38.0	47.6	45.0	43.2	33.7	<u>91.0</u>	86.7	82.9	80.2
SoftCon (Wang et al., 2024b)	ViT-Small	89.8	83.4	55.9	27.2	64.7	<u>58.7</u>	<u>52.6</u>	43.3	<u>51.1</u>	49.9	43.3	31.4	89.2	86.9	80.5	77.8
SoftCon (Wang et al., 2024b)	ViT-Base	<u>90.3</u>	82.1	54.2	19.8	63.7	<u>57.5</u>	52.0	42.5	51.0	49.7	45.3	35.4	90.0	86.1	80.6	74.5
DOFA (Xiong et al., 2024)	ViT-Base	82.8	72.1	60.9	49.6	49.4	43.6	37.2	29.9	41.4	40.7	37.5	29.4	88.3	86.2	82.0	78.3
DOFA (Xiong et al., 2024)	ViT-Large	83.6	72.1	53.5	41.7	49.9	41.6	35.3	27.6	45.4	40.6	35.6	31.8	86.8	85.2	84.8	<u>80.6</u>
Satlas (Bastani et al., 2023)	Swin-Tiny	81.7	70.3	48.3	35.8	51.9	44.8	37.8	29.6	36.6	30.7	29.6	27.1	88.2	85.2	82.4	73.0
Satlas (Bastani et al., 2023)	Swin-Base	81.5	69.1	42.1	10.0	47.0	41.1	35.0	25.8	35.8	33.4	29.6	30.4	80.0	78.3	76.9	73.3
MMEarth (Nedungadi et al., 2024)	CNN-atto	81.7	73.5	60.3	30.0	58.3	52.2	46.5	39.6	39.8	38.8	36.8	25.1	89.4	85.4	84.1	79.7
DeCUR (Wang et al., 2024a)	ViT-Small	89.0	<u>85.3</u>	72.3	46.6	<u>63.8</u>	59.2	55.4	49.6	45.8	43.1	38.5	30.9	83.7	81.7	77.9	74.2
Prithvi 2.0 (Szwarcman et al., 2024)	ViT-Large	80.2	69.4	54.1	48.0	49.4	42.9	35.5	28.8	29.5	31.2	29.6	26.1	87.9	86.8	83.3	<u>80.6</u>
AnySat (Astruc et al., 2024a)	ViT-Base	82.2	73.7	62.5	47.1	54.9	47.2	40.7	33.7	39.8	34.9	32.0	29.0	85.3	81.7	78.0	72.0
Galileo	ViT-Nano	89.7	82.4	56.6	41.7	53.8	46.3	41.5	33.9	50.1	50.3	<u>47.5</u>	<u>37.4</u>	86.7	82.2	83.2	79.7
Galileo	ViT-Tiny	90.1	83.9	59.5	41.3	55.5	48.2	41.6	34.4	49.7	<u>50.5</u>	44.2	36.2	86.9	83.7	83.8	77.3
Galileo	ViT-Base	93.0	88.5	<u>71.3</u>	56.6	59.0	51.5	45.4	36.5	54.8	53.8	51.1	43.2	90.7	86.9	<u>85.8</u>	78.0

Table 14. Image classification test performance (%) via finetuning.

Method	Arch.	m-EuroSat				m-BigEarthNet				m-So2Sat				m-Brick-Kiln			
		Training %		Top-1 Acc. \uparrow		Training %		F1 Score \uparrow		Training %		Top-1 Acc. \uparrow		Training %		Top-1 Acc. \uparrow	
		100%	20%	5%	1%	100%	20%	5%	1%	100%	20%	5%	1%	100%	20%	5%	1%
SatMAE (Cong et al., 2022)	ViT-Base	96.5	90.8	79.7	55.5	67.8	59.3	51.1	39.0	54.5	52.0	45.2	34.8	98.5	97.4	97.0	94.0
SatMAE (Cong et al., 2022)	ViT-Large	96.6	91.5	82.5	56.9	68.3	61.1	52.4	41.8	57.2	56.2	49.7	36.4	98.4	97.3	97.3	96.1
SatMAE++ (Noman et al., 2024)	ViT-Large	96.5	90.6	80.1	56.4	67.9	60.4	51.9	<u>45.6</u>	56.0	52.4	46.0	36.9	98.6	97.3	96.0	92.5
CROMA (Fuller et al., 2024)	ViT-Base	96.0	91.2	79.2	53.6	70.0	63.4	54.0	43.4	59.7	59.1	54.1	43.3	98.7	97.8	97.0	96.1
CROMA (Fuller et al., 2024)	ViT-Large	96.6	92.9	80.7	52.7	<u>71.9</u>	66.0	58.3	47.9	60.6	57.9	52.9	40.9	98.7	<u>98.0</u>	97.1	96.7
SoftCon (Wang et al., 2024b)	ViT-Small	97.4	<u>95.4</u>	84.9	57.5	69.5	62.5	53.3	36.0	61.7	<u>60.3</u>	54.2	<u>49.2</u>	98.8	98.1	<u>97.7</u>	<u>97.2</u>
SoftCon (Wang et al., 2024b)	ViT-Base	97.5	95.0	88.2	56.3	70.3	63.6	53.8	38.5	61.7	<u>60.3</u>	54.2	<u>49.2</u>	98.7	98.1	98.0	97.3
DOFA (Xiong et al., 2024)	ViT-Base	94.6	86.1	74.2	50.9	68.1	60.3	51.9	41.9	56.7	49.9	45.8	33.8	98.7	97.3	96.2	95.0
DOFA (Xiong et al., 2024)	ViT-Large	96.9	91.5	82.2	53.4	68.0	60.3	52.2	43.5	58.7	55.4	47.4	37.0	98.6	96.9	96.1	94.5
Satlas (Bastani et al., 2023)	Swin-Tiny	96.3	89.1	78.1	52.9	71.3	63.8	53.6	32.0	57.3	52.7	45.9	30.8	98.5	97.7	96.8	94.7
Satlas (Bastani et al., 2023)	Swin-Base	97.5	92.2	81.2	51.9	72.8	<u>65.1</u>	<u>54.9</u>	25.8	<u>61.9</u>	55.0	47.0	30.6	98.4	97.9	97.2	94.7
MMEarth (Nedungadi et al., 2024)	CNN-atto	95.7	86.1	73.0	47.5	70.0	62.7	<u>52.6</u>	43.4	<u>57.2</u>	51.0	44.1	30.0	98.9	<u>98.0</u>	96.5	89.2
DeCUR (Wang et al., 2024a)	ViT-Small	97.9	95.3	<u>87.9</u>	54.2	70.9	64.9	54.7	44.7	61.7	61.0	54.2	47.0	98.7	<u>98.0</u>	97.1	96.9
Prithvi 2.0 (Szwarcman et al., 2024)	ViT-Large	96.5	89.2	<u>77.6</u>	51.5	69.0	61.8	51.4	37.1	54.6	50.5	40.2	31.0	98.6	97.6	96.7	96.2
AnySat (Astruc et al., 2024a)	ViT-Base	95.9	88.2	74.4	51.3	70.3	61.6	46.1	13.3	51.8	49.8	42.0	29.7	98.6	97.2	96.8	85.6
Galileo (ours)	ViT-Nano	94.5	88.3	80.2	52.6	67.1	59.3	44.1	23.3	57.4	54.7	47.8	34.9	98.5	97.7	96.1	94.2
Galileo (ours)	ViT-Tiny	96.9	94.4	85.2	<u>60.6</u>	69.7	62.2	53.4	39.5	<u>61.9</u>	57.2	<u>54.9</u>	43.1	98.7	97.9	97.2	96.6
Galileo (ours)	ViT-Base	<u>97.7</u>	96.0	87.0	63.5	70.7	63.1	53.9	40.9	63.3	57.8	56.7	50.6	98.7	<u>98.0</u>	97.5	96.8

Table 15. Image (and image timeseries) segmentation test performance (%) via linear probing. * For semantic segmentation, AnySat outputs dense per-pixel features instead of per-patch. To keep the training-costs of the linear probes similar to other models, we sampled 6.25% of pixel features per image when training the linear probe for AnySat. Evaluation used all pixel features in an image.

Method	Arch.	m-Cashew-Plant				m-SA-Crop-Type				MADOS				Sen1Floods11				PASTIS			
		Training %, mIoU ↑				Training %, mIoU ↑				Training %, mIoU ↑				Training %, mIoU ↑				Training %, mIoU ↑			
		100%	20%	5%	1%	100%	20%	5%	1%	100%	20%	5%	1%	100%	20%	5%	1%	100%	20%	5%	1%
SatMAE (Cong et al., 2022)	ViT-Base	28.9	28.1	27.6	23.0	23.8	23.4	21.5	16.8	53.2	39.1	26.4	12.4	not supported				27.6	24.2	18.5	11.2
SatMAE (Cong et al., 2022)	ViT-Large	30.8	29.7	28.7	22.7	24.8	24.0	21.9	16.9	55.6	41.0	29.9	13.2	not supported				29.6	25.3	19.1	11.5
SatMAE++ (Noman et al., 2024)	ViT-Large	29.6	28.0	27.5	23.3	25.7	24.3	21.5	16.8	49.9	38.2	27.5	12.7	not supported				30.5	26.0	19.3	12.0
CROMA (Fuller et al., 2024)	ViT-Base	31.8	31.4	30.2	26.8	32.0	29.9	26.1	18.3	64.2	49.1	39.6	24.4	78.9	78.1	77.4	77.6	44.4	38.4	29.2	18.5
CROMA (Fuller et al., 2024)	ViT-Large	34.3	33.3	<u>32.5</u>	<u>27.9</u>	32.0	29.9	<u>25.6</u>	18.0	<u>66.3</u>	52.5	<u>36.2</u>	13.9	78.6	78.0	77.1	77.2	42.9	35.9	25.8	16.1
SoftCon (Wang et al., 2024b)	ViT-Small	27.0	26.8	25.6	23.0	28.5	27.8	24.3	17.7	57.1	44.0	29.4	19.1	78.5	78.3	76.9	75.6	28.6	26.1	19.3	11.8
SoftCon (Wang et al., 2024b)	ViT-Base	29.6	28.9	27.2	22.8	<u>30.8</u>	<u>29.3</u>	24.7	<u>18.5</u>	60.3	42.4	31.9	16.5	78.0	77.4	74.9	74.8	31.3	26.5	19.3	10.5
DOFA (Xiong et al., 2024)	ViT-Base	26.9	26.7	26.8	22.2	24.8	23.9	21.0	16.6	48.3	37.4	30.0	19.1	78.1	77.8	77.0	77.1	29.8	25.6	19.5	13.2
DOFA (Xiong et al., 2024)	ViT-Large	27.7	27.4	27.3	23.3	25.4	23.9	21.3	16.8	51.6	38.5	31.0	<u>19.1</u>	78.1	77.9	77.3	77.4	29.8	25.5	19.5	13.4
Satlas (Bastani et al., 2023)	Swin-Tiny	25.1	24.8	24.2	18.6	23.4	22.7	19.8	16.2	45.9	35.7	26.5	12.4	not supported				28.0	24.0	17.4	10.9
Satlas (Bastani et al., 2023)	Swin-Base	24.5	24.4	23.3	19.4	22.4	21.6	19.3	14.7	48.0	36.5	25.9	15.9	not supported				25.4	21.6	16.1	9.2
MMEarth (Nedungadi et al., 2024)	CNN-atto	24.2	24.6	24.6	20.3	22.2	21.0	18.7	14.1	34.2	26.4	19.5	16.1	not supported				24.0	21.6	16.0	10.5
DeCUR (Wang et al., 2024a)	ViT-Small	26.2	26.2	26.0	22.8	21.5	20.8	19.2	15.3	54.8	40.9	30.3	16.6	74.5	74.6	73.5	72.2	22.4	19.7	15.4	11.0
Prithvi 2.0 (Szwarcman et al., 2024)	ViT-Large	26.7	26.6	26.8	23.2	22.9	22.3	20.3	15.7	50.0	41.8	33.7	18.9	not supported				29.3	26.8	20.2	13.2
AnySat* (Astruc et al., 2024a)	ViT-Base	26.1	26.1	24.9	21.7	27.1	25.2	21.4	15.8	50.2	39.8	30.5	17.0	77.9	77.6	77.1	76.9	46.2	41.9	33.7	23.5
Galileo	ViT-Nano	24.4	24.6	24.6	24.5	19.7	19.7	17.1	14.5	54.8	41.4	28.9	13.9	78.6	<u>78.5</u>	<u>77.7</u>	77.1	17.5	17.0	15.7	13.1
Galileo	ViT-Tiny	27.4	27.0	27.3	<u>27.9</u>	22.5	22.4	20.5	17.1	60.8	<u>50.6</u>	34.0	17.5	78.0	<u>77.8</u>	<u>77.7</u>	<u>77.9</u>	28.1	27.0	23.1	16.9
Galileo	ViT-Base	<u>33.0</u>	<u>32.8</u>	33.1	30.2	30.1	<u>29.3</u>	25.4	19.4	67.6	49.0	34.1	14.7	79.4	79.0	78.5	78.2	39.2	36.7	27.9	<u>18.7</u>

Table 16. Model rankings, computed against the full Image Classification (Im. Class.) results in Table 13, Image Segmentation (Im. Seg.) results in Table 15 and TimeSeries (TS) results in Table 6. We aggregate the Image Classification and Image Segmentation rankings into a single “Image” (Im.) rankings. When we do this, we average the rankings across all the tasks (as opposed to naively averaging the aggregated image classification and image segmentation rankings).

Method	Arch.	Im. Class.		Im. Seg	Im.	TS
		KNN	FT	LP		
SatMAE (Cong et al., 2022)	ViT-Base	13.8	12.5	11.7	12.6	N/A
SatMAE (Cong et al., 2022)	ViT-Large	11.9	9.1	10.1	10.4	N/A
SatMAE++ (Noman et al., 2024)	ViT-Large	10.9	11.4	10.4	10.9	N/A
CROMA (Fuller et al., 2024)	ViT-Base	<u>3.6</u>	7.4	2.5	<u>4.3</u>	N/A
CROMA (Fuller et al., 2024)	ViT-Large	5.9	5.3	3.5	4.8	N/A
SoftCon (Wang et al., 2024b)	ViT-Small	5.6	4.7	7.7	6.1	N/A
SoftCon (Wang et al., 2024b)	ViT-Base	5.9	4.0	7.3	5.9	N/A
DOFA (Xiong et al., 2024)	ViT-Base	9.4	13.1	9.6	10.6	N/A
DOFA (Xiong et al., 2024)	ViT-Large	10.6	10.2	7.7	9.4	N/A
Satlas (Bastani et al., 2023)	Swin-Tiny	12.7	10.6	14.9	12.9	N/A
Satlas (Bastani et al., 2023)	Swin-Base	15.9	7.9	15.7	13.4	N/A
MMEarth (Nedungadi et al., 2024)	CNN-atto	8.3	11.7	16.1	12.3	N/A
DeCUR (Wang et al., 2024a)	ViT-Small	7.0	<u>3.6</u>	13.0	8.3	N/A
Prithvi 2.0 (Szwarcman et al., 2024)	ViT-Large	12.0	12.5	10.8	11.7	N/A
AnySat (Astruc et al., 2024a)	ViT-Base	11.1	14.5	8.3	11.1	4.5
Presto (Tseng et al., 2023)	ViT-Presto	N/A	N/A	N/A	N/A	3.0
Galileo	ViT-Nano	7.0	13.1	12.2	10.9	3.5
Galileo	ViT-Tiny	6.6	5.8	6.8	6.4	<u>2.3</u>
Galileo	ViT-Base	2.9	3.5	<u>2.7</u>	3.0	1.8